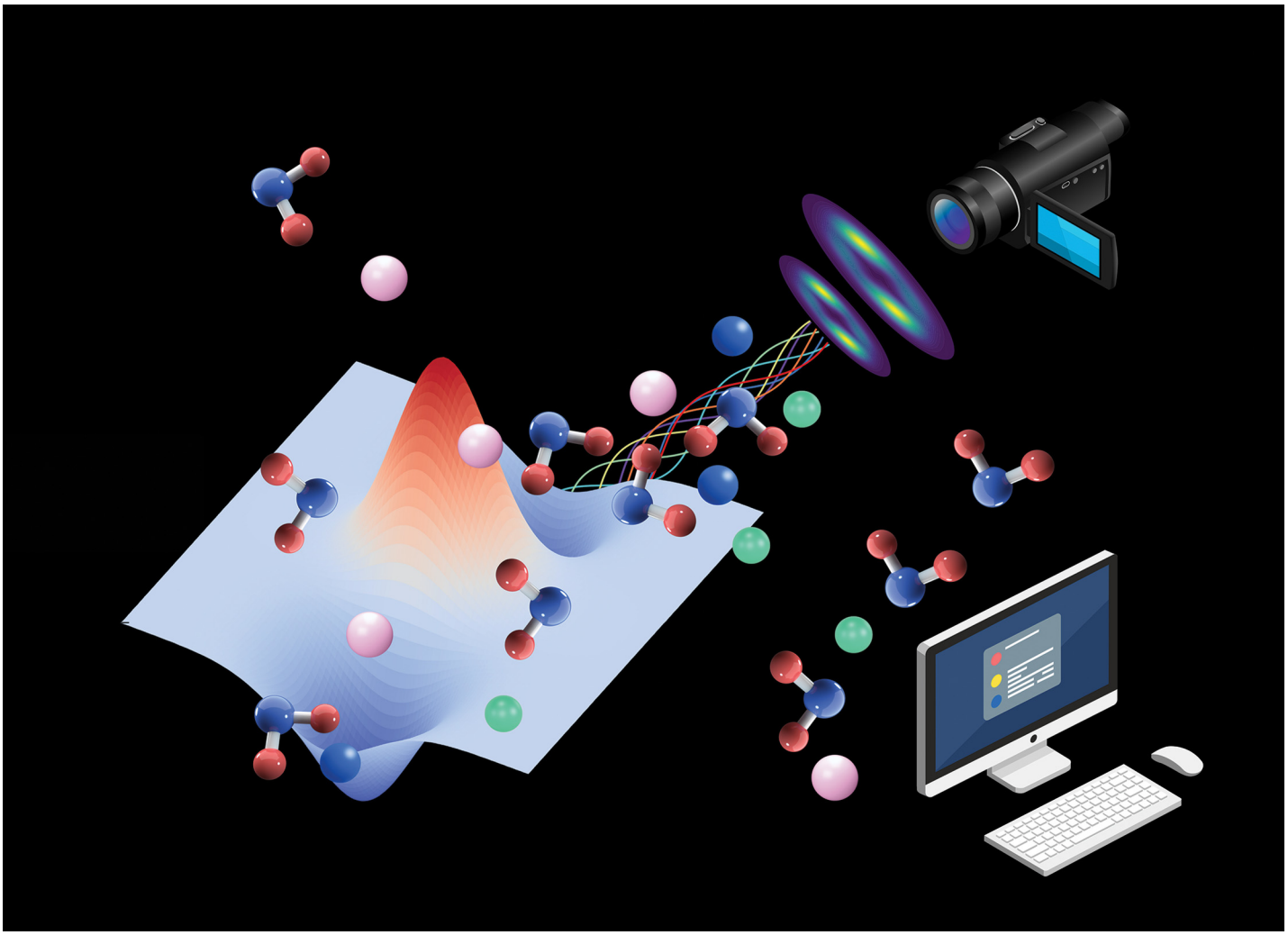

Showcasing research from the groups of Thierry Stoecklin, Institut des Sciences Moléculaires, Université de Bordeaux, Bordeaux, France, and Zhong-Fa Sun and David H. Parker, Department of Physics, Anhui Normal University, Anhui, China.

A comprehensive study of the differential cross sections for water–rare gas collisions: experimental and theoretical perspectives

Using crossed molecular beams, velocity map imaging, and quantum scattering calculations on precise potential energy surfaces, this study explores water–rare gas collisions (Ne, Ar, Xe). Experimental results align well with theory, showing cross sections increasing with rare gas mass due to stronger interactions. Angular distribution oscillations highlight short-range repulsion, confirming collision dynamics are dominated by the interaction potential's repulsive component.

Image reproduced by permission of Ricardo Manuel García-Vázquez from *Phys. Chem. Chem. Phys.*, 2025, **27**, 12139.

As featured in:

See Ricardo Manuel García-Vázquez, Zhong-Fa Sun, David H. Parker, Thierry Stoecklin *et al.*, *Phys. Chem. Chem. Phys.*, 2025, **27**, 12139.

ROYAL SOCIETY OF CHEMISTRY

rsc.li/pccp

Registered charity number: 207890

PCCP Owner Societies

PCCP

PAPER

View Article Online
View Journal | View Issue

Cite this: *Phys. Chem. Chem. Phys.*, 2025, **27**, 12139

A comprehensive study of the differential cross sections for water–rare gas collisions: experimental and theoretical perspectives

Ricardo Manuel García-Vázquez, *[a] Zhong-Fa Sun, *[b] Chung-Hsin Yang, [c] Lisán David Cabrera-González, [d] Otoniel Denis-Alpizar, [e] Philippe Halvick, [a] David H. Parker *[bf] and Thierry Stoecklin *[a]

Received 23rd December 2024,
Accepted 17th March 2025

DOI: 10.1039/d4cp04825c

rsc.li/pccp

Experimental measurements and theoretical quantum calculations of the inelastic differential cross sections for the collisions of H_2O with Ne, Ar and Xe atoms are respectively compared at the 364, 390 and 351 cm^{-1} collision energies. The four rotational excitation transitions $0_{00} \rightarrow 1_{11}$, $1_{01} \rightarrow 2_{12}$, $1_{01} \rightarrow 1_{10}$ and $1_{01} \rightarrow 2_{21}$ are studied for the three systems. The experimental setup consists of a crossed molecular beam machine with velocity map imaging complemented with state-selective laser ionization detection. The theoretical approach is based on close-coupling calculations of rare gas scattering by rigid H_2O, using two recently developed potential energy surfaces for Ne + H_2O and Ar + H_2O systems as well as a new potential energy surface developed in this work for the Xe + H_2O system. Measured and calculated differential cross sections are in good agreement. The integral cross section is increasing in proportion to the mass of the rare gas atom. This can be attributed to the rise of the rare gas polarizability along with the rise of the dissociation energy and reduced mass of the Rg–H_2O complex. The fast oscillations observed in the calculated differential cross sections attest that the collision dynamics is mainly driven by the repulsive part of the interaction potential, as could be expected since the collision energies are much larger than the dissociation energies.

1 Introduction

Differential cross sections (DCSs) give the most detailed information about a collisional process and this is the reason why so many comparisons between theoretical and experimental DCSs are performed. They are a sensitive test for the accuracy of the interaction energy model. Such comparison can be quite fruitful as demonstrated for example by the study recently performed by Xiahou *et al.* for the F+ H_2 reactive collision.[1] The evaluation of DCS for inelastic collisions of atoms with symmetric[2] or asymmetric top molecules[3] has recently been the subject of renewed interest, largely due to the advent of ion imaging techniques. Water has been the subject of such studies due to its presence in various environments and its significant role in atmospheric physics and astrochemistry. DCSs for elastic scattering of H_2O with the rare gases, H_2, and H_2O were first acquired by Bickes *et al.*[4] In their pioneering work, the observed diffractive oscillations and rainbow maximum were employed to fit the parameters of the assumed Lennard-Jones model potential such as the well depth and the location of potential minimum. Later on Slankas *et al.*[5] performed a similar experiment for H_2O colliding with He and demonstrated that both the attractive and repulsive part of the potential were less anisotropic than expected. A more detailed measurement of the elastic differential cross sections for H_2O + He at two different collision energies was carried out by Brudermann *et al.* using time-of-flight analysis of the scattered He atoms. They also compared the measured rotationally inelastic cross sections with quantum calculations.[6] However those measurements obtained by angle-dependent energy-loss spectra did not allow state selectivity.

Rotationally resolved state-to-state integral cross sections for collisions of *ortho* and *para*-H_2O with Ar were also investigated

[a] *Univ. Bordeaux, CNRS, Bordeaux INP, ISM, UMR 5255, F-33400 Talence, France. E-mail: rgarciavazqu@u-bordeaux.fr, thierry.stoecklin@u-bordeaux.fr*
[b] *Anhui Province Key Laboratory for Control and Applications of Optoelectronic Information Materials, Department of Physics, Anhui Normal University, Wuhu, Anhui 241002, China. E-mail: zfsun@ahnu.edu.cn*
[c] *Institute of Atomic and Molecular Sciences, Academia Sinica, Taipei 10617, Taiwan*
[d] *Department of Chemistry, The University of Manchester, Oxford Road, Manchester, M13 9PL, UK*
[e] *Departamento de Física, Facultad de Ciencias, Universidad de Chile, Av. Las Palmeras 3425, Ñuñoa, Santiago, Chile*
[f] *Department of Molecular and Laser Physics, Institute for Molecules and Materials, Radboud University, Heyendaalseweg 135, 6525 AJ Nijmegen, The Netherlands. E-mail: parker@science.ru.nl*

by the Nesbitt group.[7] In their work, the measured integral cross sections was found to display an exponential-decay dependence with the magnitude of the rotational energy transfer, approximately following an energy gap law. They also observed a clear propensity for rotational excitation of H_2O around the *a* and *c* principal axes. Glory structures in the total cross sections for H_2O–rare gas collisional systems were then identified by Cappelletti and coworkers.[8,9]

Recently, the rotationally inelastic collision process for H_2O + He at 429 cm^{-1} collision energy was studied through the velocity map imaging technique in combination with resonant enhanced multiphoton ionization detection by Yang and coworkers.[10,11] The state-to-state DCSs were extracted experimentally for the first time from the measured images and found to be in good agreement with full close-coupling quantum calculations based on an *ab initio* potential. New measurements were subsequently performed for this system using the same imaging techniques[12] at collision energies ranging from 381 to 763 cm^{-1} by step of approximately 100 cm^{-1}. In addition to He as a collision partner, an imaging study of H_2O in collision with H_2 was also conducted by Yang *et al.*[13] The H_2O–H_2 and H_2O–He DCSs were found to differ strongly for both normal-H_2 and *para*-H_2 beams. Forward scattering was found to be favoured for all rotational states of H_2, indicating that the H_2O–H_2 potential well is deeper. The standard procedure of estimating rates for *para*-H_2 collisions using those obtained for He in astrochemistry should then be applied with caution.

Here we compare rotational state-to-state resolved DCS for the collisions of H_2O in the rovibrational ground-state with Ne, Ar and Xe at respectively 364, 390 and 351 cm^{-1}. The same four $0_{00} \rightarrow 1_{11}$, $1_{01} \rightarrow 2_{12}$, $1_{01} \rightarrow 1_{10}$ and $1_{01} \rightarrow 2_{21}$ rotational excitation transitions are studied for the three systems using a combined experimental and theoretical approach. The selection of these three chemically similar collision partners of water aims to investigate the impact of an increase in the relative mass and the potential well depth of the potential energy surface (PES). The experimental setup employed is a crossed-beam apparatus, complemented with velocity-map imaging detection. Single final rotational states of *ortho* and *para*-H_2O molecules before and after collisions are detected by a 2 + 1 resonance enhanced multi-photon ionization (REMPI) process and the state-to-state DCSs measured using the velocity-map imaging (VMI) method.

Two recently developed and tested PESs are used to perform the close-coupling calculations for the Ne + H_2O[14] and Ar + H_2O[15] scatterings while a new PES is developed in this work for the Xe + H_2O scattering. The last PES is tested by calculating the bound states of the Xe + H_2O system as well as its transition frequencies, which are compared with experiments and with previous calculations.

The manuscript is organised in two main sections dedicated to the presentation of the methods and the results. Each of the aforementioned principal sections is subdivided into two sections, one pertaining to the experiment and the other to the theory. A concluding section is also eventually included, in which a few final remarks are presented.

2 Methods

2.1 Experimental methods

The water molecule–rare gas atom rotationally inelastic collision experiments were carried out on a home-built crossed beam VMI apparatus (see Fig. 1). Full details of the apparatus[10,12,13,16] and the nascent water laser ionization detection method[11] have been described respectively in the previous publications, thus only a brief description is given in this section. In short, the experiments employed two differentially pumped molecular beams in two separated source chambers, a VMI setup inside a collision chamber and a laser beam for ionization detection.

The primary beam was achieved by flowing pure Ar gas (~1 bar) into a H_2O bubbler (demineralized water at room temperature) and then through a commercial hairpin-type pulsed valve (Jordan Inc.), resulting in a H_2O molecular beam with a concentration of H_2O being ~2.5%. Due to adiabatic expansion, the H_2O beam was rotationally cooled to ~12 K, where more than 97% of *para*-H_2O and 90% of *ortho*-H_2O are populated in the lowest 0_{00} and 1_{01} rotational levels in the ground vibrational state, respectively. The secondary beam (Ne, Ar, Xe) was produced at ~1 bar stagnation pressure by a second Jordan valve located in the other source chamber. Both pulsed valves had a nozzle diameter of 0.5 mm and were operated at 10 Hz, generating pulses with a duration of around 100 μs. The primary and secondary beam were collimated respectively by a skimmer of 2.5 mm diameter positioned 30 mm downstream from its corresponding valve nozzle, and crossed each other with a collision angle of 90° at the reaction

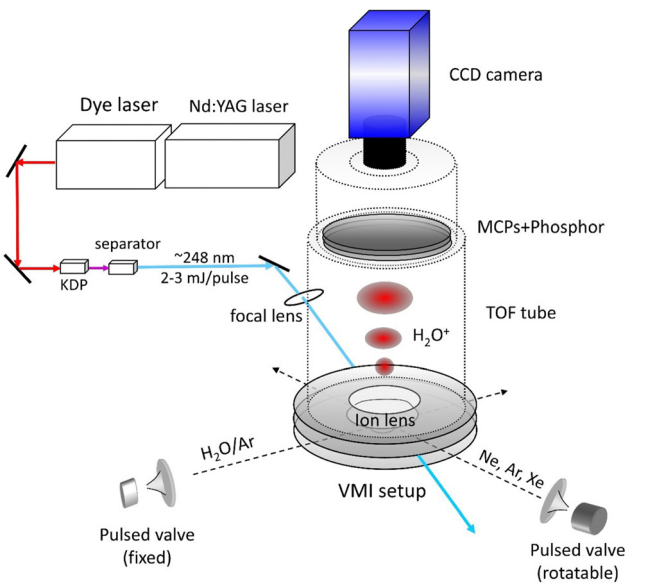

Fig. 1 Schematic diagram of the crossed-beam VMI apparatus. Pulsed molecular beams of 2.5% H_2O/Ar and neat rare gas (Ne, Ar, Xe) are skimmed and crossed at 90°. The collision-induced rotationally excited H_2O is state-selectively ionized *via* (2 + 1) REMPI by laser radiation in the 248 nm region produced by a pulsed tunable dye laser beam doubled in a KDP crystal. The mass-selected H_2O^+ ions are velocity-mapped by a VMI setup and projected onto a two-dimensional detector, then recorded by a CCD camera.

center of the VMI stack, which was 90 mm downstream from both valves. The VMI setup was positioned in the center of the collision chamber with the ion optics and time-of-flight tube perpendicular to the collision plane defined by the two molecular beams. The mean collision energies in the center of mass frame of the Ne + H_2O, Ar + H_2O and Xe + H_2O collision system, 364, 390 and 351 cm^{-1}, were determined from the velocity mapped beam spot positions of two beams (for the secondary beam velocity determination a trace amount of H_2O was seeded in the pure rare gas (Rg) beam) and again confirmed by the variation in radius of the scattering image as a function of the rotationally excited H_2O internal energy after collision.

After collision, the rotationally excited nascent H_2O molecules were state selectively ionized by (2 + 1) resonance enhanced multiphoton ionization (REMPI) using laser radiation $\sim$248 nm, that was generated by a tunable dye laser system (Lambda Physik Scanmate) pumped by the third harmonic of a pulsed Nd:YAG laser (Contiuum Powerlite 9010). Both molecular beams and the detection laser beam were coplanar. The laser beam with a typical power of 2–3 mJ per pulse was focused by a 20 cm focal lens to the center of the collision region. H_2O^+ ions were velocity mapped by the VMI setup and then projected onto a position sensitive imaging detector consisting of dual MCP and a phosphor screen, with mass selectivity obtained by applying a pulse voltage on the MCP at the appropriate moment. The velocity mapped ion images appearing on the phosphor screen were subsequently recorded by a CCD camera. Typically, 20 000 laser shots were averaged for each image, under interleaved conditions with and without the Rg beam in temporal overlap with the H_2O beam; the second condition achieved through delaying the Rg beam by 1 ms with respect to the H_2O beam was used for background subtraction.

The state-to-state DCSs were extracted from the density-to-flux corrected velocity mapped images of nascent H_2O^+ that were experimentally measured. A detailed description of image corrections and the extraction of DCSs has been presented in previous publications.[10,12,13,16–19] During our experiments, we have checked the influence in the images of the direction of the linear polarization electric field vector of the detection laser. We did not find observably difference in the images. We therefore ignore collision-induced alignment effects in our H_2O scattering image analysis procedure.

2.2 Theoretical methods

2.2.1 Potential energy surfaces. To properly describe the inelastic scattering of water with Ne, Ar, and Xe we need accurate PESs. In the case of collisions with Ne and Ar, our recently developed PESs[14,15] are employed, whereas for those with Xe, a new PES was derived through the fit of a substantial set of *ab initio* points.

The *ab initio* calculations were performed using MOLPRO 2015[20] at the explicitly correlated coupled-cluster level of theory, including single, double, and perturbative triple excitations (CCSD(T)-F12). For the hydrogen and oxygen atoms, the aug-cc-pVQZ basis set was employed, whereas for the xenon atom, the pseudopotential aug-cc-pVQZ-PP basis set was utilised. A set of bond functions, comprising 3s, 3p, 2d, 2f and 1g orbitals,[21] was located at the midpoint of the internuclear distance, R, to complement the polar-diffuse basis set.

The H_2O molecule is assumed to be rigid and the relative position of the xenon is defined by the spherical coordinates R, θ, φ with the origin fixed at the H_2O center of mass. The grid includes 28 radial points in the [2.8, 30.0] Å interval, 13 values of θ in the [0°, 180°] interval in steps of 15°, as well as 7 values of φ between 0° and 90° in steps of 15° giving a total of 2548 *ab initio* points. The OH distance and the bending angle were fixed to their vibrationally averaged values, r_{OH} = 0.9753 Å and γ_{HOH} = 104.41°.[22] Following the same methodology used in some of our previous works,[15] the grid of *ab initio* energies was divided into two parts, the short range (SR) for $R < 10$ Å and the long range (LR) for $R \geq 10$ Å. The SR and LR grids were expanded in the Green angular basis set:[23]

$$V(R,\theta,\varphi) = \sum_{m=0}^{m_{max}} \sum_{l=m}^{l_{max}} \upsilon_{l,m}(R) \bar{P}_l^m(\cos\theta)\cos(m\varphi), \quad (1)$$

using l_{max} = 10 and m_{max} = 8 for the SR expansion and l_{max} = 4 and m_{max} = 2 for the LR expansion. Due to the water molecule's C_{2v} symmetry, the summation over m is restricted to even values of m. For each value of R included in each grid (R_i), the coefficients $\upsilon_{l,m}(R_i)$ were computed using the least square method. These coefficients were later fitted using the Reproducing Kernel of the Hilbert Space (RKHS) polynomials:

$$\upsilon_{l,m}(R) = \sum_{i=1}^{N_R} \alpha_i^{l,m} q^{2,5}(R, R_i) \quad (2)$$

where N_R is the number of R values included in the grid and $q^{2,5}(R, R_i)$ is the one-dimensional radial kernel:[24]

$$q^{2,5}(R, R_i) = \frac{2}{21R_>^6} - \frac{R_<}{14R_>^7} \quad (3)$$

in which $R_<$ = min(R, R_i) and $R_>$ = max(R, R_i). The $\alpha_i^{l,m}$ coefficients were determined by solving the linear equation system $\mathbf{q}(R, R_{i'})\alpha^{l,m} = \upsilon_{\mathbf{l,m}}(R_i)$, where i and i' label different radial configurations of the grid. The selection of the $q^{2,5}$ kernel ensures the long range's van der Waals R^{-6} behaviour for $R > 30$ Å. The final PES is obtained by combining the two fits using a switching function, as described by eqn (5) and (6) of our previous work[15] with a smoothing parameter A_0 = 6 $Å^{-1}$.

2.2.2 Scattering calculations. All the scattering calculations as well as the bound states calculations for Xe–H_2O are performed in the space fixed (SF) frame which origin is fixed at the H_2O center of mass. Water is lying in the x–z molecule-fixed plane with the z-axis bisecting the HOH angle while the Ne/Ar/Xe projectile are described using spherical coordinates R, θ, φ. (See Fig. 1 of ref. 14 and 15). In a series of recent studies, we have examined the collisions of H,[25] He,[26] and Ar[15] with H_2O in excited vibrational levels. Our findings, presented in these studies, indicate that the rotational transitions within the fundamental vibrational level are accurately captured by the rigid rotor approximation, a conclusion that holds for the collision energy range considered in the present study. These findings have been

corroborated in other studies of the H_2O + Ar inelastic collision[27,28] and are not only valid for the calculation of cross-section but also for the study of bound states of water + He systems. For example, the bound states calculated in our previous work[26] using the rigid rotor and the rigid bender approximations are in excellent agreement with the ones reported by Hou *et al.*,[29] calculated from the full dimensional PES reported in the same work. Then, the rigid-rotor atom-asymmetric top close-coupling equations[23] are solved using the NEWMAT code.[30] The last version of this code, which allows calculating the DCS, was recently applied to the calculation of the DCS for the collisions of Ne with H_2O, HDO and D_2O.[31] We here briefly remind the main notations used for the DCS calculations. The H_2O rotational wave function is, as usual, a linear combination of symmetric top wave functions ($|jkm\rangle$):

$$|j\tau m,p\rangle = \sum_{\bar{k}\geq 0} N_{\bar{k}} a^{j}_{\tau,\bar{k}}\left[|j\bar{k}m\rangle + (-1)^{p}|j-\bar{k}m\rangle\right], \qquad (4)$$

where $\bar{k}$ is the absolute value of k, p is a symmetrization factor[32] such that $p = 0$ for $\bar{k} = 0$ and $p = 0, 1$ for $\bar{k} > 0$, $N_{\bar{k}} = \dfrac{1}{\sqrt{2\left(1+\delta_{\bar{k},0}\right)}}$ is a normalization factor while k and m are the projection of the H_2O rotational angular momentum $\vec{j}$ respectively along the molecule-fixed z-axis and the SF z-axis. The τ index labels the $2j + 1$ asymmetric top levels inside a given j multiplet. We indifferently use the alternative notation $j_{k_a k_c}$ where k_a and k_c refer to the $\vec{j}$ projection over the a and c molecular axes and $\tau = k_a - k_c$. The expansion coefficients $a^{j}_{\tau,\bar{k}}$ as well as the eigenenergies ($\varepsilon_{j,\tau}$) are as usual obtained from the diagonalization of the rigid-rotor asymmetric top Hamiltonian:

$$H_{\mathrm{rot}} = A_x j_x{}^2 + A_y j_y{}^2 + A_z j_z{}^2, \qquad (5)$$

in the basis set eqn (4) where $A_x = A$, $A_y = C$ and $A_z = B$ while A, B and C are the spectroscopic constant of the water molecule.[33]

The angular wavefunction describing the relative movement of the impinging atom in the SF frame is a spherical harmonic $Y_l^{m_l}(\hat{R})$ where $\hat{R} = (\varphi,\theta)$ while l, m_l are respectively the quantum numbers associated with the relative angular momentum $\vec{l}$ and its projection along the SF z-axis. The quantum numbers associated with the total angular momentum ($\vec{J} = \vec{j} + \vec{l}$) and its projection along the SF z-axis are denoted J and M. The angular basis set of the collisional system is obtained by coupling the $Y_l^{m_l}(\hat{R})$ and $|j\tau m,p\rangle$ functions using the Wigner Eckart theorem:

$$|j\tau,p,l;JM\rangle = \sqrt{\frac{2J+1}{4\pi}} \sum_{m,m_l} \langle jm,lm_l \mid JM\rangle |j\tau m,p\rangle\, Y_l^{m_l}(\hat{R}). \quad (6)$$

The DCS for the inelastic collision between the Rg and H_2O are calculated using the formula:

$$\frac{\mathrm{d}\sigma}{\mathrm{d}\hat{R}}\left(j'\tau' \leftarrow j\tau|\hat{R}\right) = \frac{k_{j'\tau'}}{(2j+1)k_{j\tau}} \sum_{m=-j}^{j} \sum_{m'=-j'}^{j'} \left|f\left(j'm'\tau' \leftarrow jm\tau|\hat{R}\right)\right|^2 \qquad (7)$$

where the prime indexes designate the final states of the molecule and $k_{j\tau} = \sqrt{2\mu\left(E-\varepsilon_{j\tau}\right)}$. The scattering amplitude $f(j'm'\tau' \leftarrow jm\tau|\hat{R})$, for the case of an atom colliding with a rigid asymmetric molecule, is defined as:

$$\begin{aligned} f\left(j'm'\tau' \leftarrow jm\tau|\hat{R}\right) &= \\ &\sqrt{\frac{\pi}{k_{j'\tau'}k_{j\tau}}} \sum_{Jll'} i^{l-l'+1}(-1)^{j+j'-l-l'} \\ &\times (2J+1)\sqrt{2l+1} \begin{pmatrix} j & l & J \\ m & 0 & -M \end{pmatrix} \begin{pmatrix} j' & l' & J \\ m' & m_{l'} & -M \end{pmatrix} \\ &\times T^{J}_{j\tau l;j'\tau' l'} Y_{l'}^{m_{l'}}(\hat{R}) \end{aligned} \qquad (8)$$

where $T^{J}_{j\tau l;j'\tau' l'}$ is the transition matrix obtained from the close-coupling calculations and $M = m$, $m_{l'} = m - m'$ due to the properties of the $3-j$ symbols.

For the three systems investigated, the H_2O rotational basis set used to perform the close-coupling calculations included ten values of j, namely $0 \leq j \leq 9$. The calculations were furthermore performed separately for the *para* and *ortho* forms, using the log-derivative propagator[34,35] with $R \in [3,20]a_0$ interval for Ne, $R \in [3,40]a_0$ interval for Ar and $R \in [5.5,50]a_0$ interval for Xe, with a step size of $0.1a_0$. The convergence was checked as a function of the step size and of the maximum propagation distance. The relative convergence of the total inelastic cross section as a function of J was taken to be better than 10^{-6}, leading to maximum values 108, 146, and 161 of J for the collisions with Ne, Ar and Xe, respectively. While these maximum values of J satisfy to the high relative convergence criterion imposed to the total inelastic cross sections, particular state-to-state transitions may require a lower number of partial waves to be converged at the same relative criterion. The values of partial waves needed to achieve the 10^{-6} relative convergence criteria, for the four transitions of interest and for each of the three systems are reported in Table 1.

2.3 Bound states calculation of the Xe–H_2O system

The bound states were calculated using the same variational approach that we have previously utilized and detailed in recent works.[14,15,26,36] Briefly, the wave function of the system is expanded in the angular basis set used for the scattering calculations (eqn (6)) in order to obtain the radial equations. The latter are then solved variationally by utilizing a 200-points Chebyshev Discrete Variable Representation (DVR) in the $[5.5,50]a_0$ interval. The bound states are labeled using the notation $nK(j_{k_a k_c})^{\mathrm{e/f}}$ where n is the van der Waals stretch mode and K is the projection of $\vec{j}$ on the body-fixed z-axis. K takes the integer values 0, 1, 2,... denoted by the Greek letters Σ, Π, Δ, ... The notation $j_{k_a k_c}$ refers to the rotational states of the H_2O molecule and the spectroscopic parity is represented by the symbols e/f.

Table 1 Maximum value of the total angular momentum needed to converge the state-to-state inelastic cross section with a relative criterion of 10^{-6}

	J_{max}		
Transitions	Ne–H_2O	Ar–H_2O	Xe–H_2O
$0_{00} \rightarrow 1_{11}$	91	114	130
$1_{01} \rightarrow 1_{10}$	107	145	160
$1_{01} \rightarrow 2_{12}$	82	103	112
$1_{01} \rightarrow 2_{21}$	57	71	83

3 Results

3.1 Xe–H_2O PES

The root mean square deviation (RMSD) is used to check the quality of the fit. We divided our *ab initio* grid into three subsets associated respectively with negative energies, positive energies below 1000 cm^{-1} and positive energies in the [1000, 10 000] cm^{-1} interval. The RMSD values in these three intervals are respectively 4.32×10^{-3} cm^{-1}, 1.55×10^{-2} cm^{-1} and 0.13 cm^{-1} demonstrating the good accuracy of the fit.

Contour plots of the PES in Cartesian coordinates (x, z) for $\varphi = 0^\circ$ and (y, z) for $\varphi = 90^\circ$ are presented in the right and left panels of Fig. 2 respectively. The global minimum and the three saddle points are identified by red points and crosses, respectively. The geometries and energies of these three critical points are compared with those reported in previous studies in Table 2. The geometries are seen to be in very good agreement, while our well depth is larger as our *ab initio* calculations include more correlation contributions.

3.2 Xe–H_2O bound states

The bound states of the system were calculated for the two spin modifications (*ortho*/*para*) of the water molecule and for six values of its rotational angular momentum ($0 \leq j \leq 5$). In order to check the accuracy of our new Xe–H_2O PES, we compare in Table 3 the bound states energies with those reported in Table 2 of ref. 37. As the number of bound states is quite numerous, we limit the comparison to the first and final bound states of each of the four symmetry blocks (combination of *ortho*/*para* and parity inversion e/f). We give both our calculated values as well as the differences with the results of ref. 37. As can be seen in Table 3, our energies are systematically deeper than those calculated by Wang and Yang[37] by about 3 cm^{-1} (between $\sim$2.8 cm^{-1} to $\sim$3.9 cm^{-1}) as a result of the deeper well depth of our PES by about 3 cm^{-1}. A comparison of the transitions frequencies calculated by us and those reported in ref. 37 with the experimental values available in ref. 38 is also presented in Table 4 inside the $\Sigma(0_{00})^e$ and $\Sigma(1_{01})^e$ symmetry blocks for the most abundant isotope (^{132}Xe–H_2 ^{16}O). Our results are in excellent agreement with those of previous theoretical and experimental studies.[37,38] The present frequencies are in slightly better agreement with experiment than those calculated by Wang and Yang[37] as the largest relative error is 1.4%, for the $\Sigma(1_{01})^e$ J'–J'' = 4-3 transition while it is 1.9% for the all the $\Sigma(0_{00})^e$ transitions reported in ref. 37.

Table 2 Comparison of the geometries and energies of the global minimum and saddle points of the Xe–H_2O PES computed in the present work with those obtained by Wang and Yang[37] and Wen and Jäger.[38] Distances are reported in Å and energies in cm^{-1}

	This work	Ref. 37	Ref. 38
Global minimum			
R	4.02	4.00	4.00
θ	119.50°	120.00°	120.00°
φ	0.00°	0.00°	0.00°
V	−195.44	−192.50	−191.70
First-order saddle point 1			
R	3.98	3.95	3.95
θ	180.00°	180.00°	180.00°
φ	0.00°	0.00°	0.00°
V	−169.34	−169.20	−169.10
First-order saddle point 2			
R	3.83	3.85	3.85
θ	0.00°	0.00°	0.00°
φ	0.00°	0.00°	0.00°
V	−168.25	−161.3	−161.5
Second-order saddle point 2			
R	3.96	3.95	4.00
θ	99.50°	95.00°	100.00°
φ	90.00°	90.00°	90.00°
V	−134.06	−130.30	−130.10

3.3 Integral cross sections

Before commenting on the scattering results it is interesting to recall the physical interpretation introduced by Chapman *et al.*[7] to classify the asymmetric top states of the water molecule. For

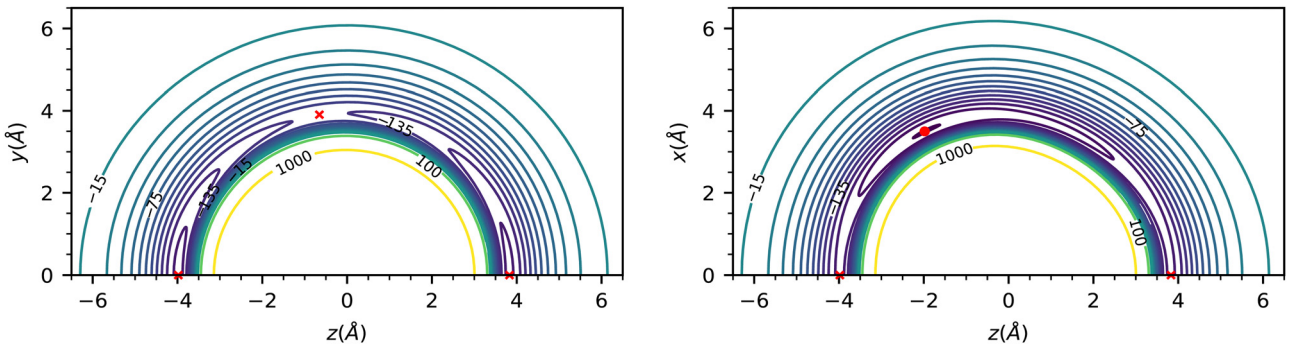

Fig. 2 Contour plots for the H_2O–Xe PES. The right panel shows the x–z contour plot for $\varphi = 0^\circ$ ($y = 0$ plane) while the left panel shows the y–z contour plot for $\varphi = 90^\circ$ ($x = 0$ plane).

Table 3 Bound state energies in cm^{-1} of the Xe–H_2O system calculated in the present work (TW). The energy differences between our results and those given in Table 2 of ref. 37 are also reported (TW–WY). Only the first and the last bound states of each of the four symmetry blocks are presented

Assignment	$J = 0$	TW–WY	$J = 1$	TW–WY	$J = 2$	TW–WY	$J = 3$	TW–WY	$J = 4$	TW–WY
Xe–$p$$H_2O$										
$\Sigma(0_{00})^e$	−143.361	−3.424	−143.226	−3.423	−142.957	−3.421	−142.553	−3.419	−142.014	−3.415
$\Delta(2_{02})^e$					−49.879	−3.936	−49.506	−3.938	−49.009	−3.942
$\Pi(1_{11})^f$			−105.893	−3.493	−105.625	−3.493	−105.221	−3.491	−104.682	−3.487
$\Delta(2_{02})^f$					−18.680	−3.340	−18.305	−3.382	−17.804	−3.419
Xe–$o$$H_2O$										
$\Sigma(1_{01})^e$	−126.895	−3.559	−126.763	−3.558	−126.499	−3.557	−126.103	−3.555	−125.575	−3.552
$3\Sigma(1_{01})^e$	−40.787	−3.188	−41.043	−3.443	−40.812	−3.429	−40.466	−3.412	−40.005	−3.393
$\Pi(1_{01})^f$			−115.059	−3.019	−114.791	−3.015	−114.389	−3.010	−113.854	−3.003
$2\Sigma(1_{10})^f$	−27.310	−2.81	−27.191	−2.808	−26.954	−2.806	−26.599	−2.802	−26.126	−2.798

Table 4 Comparison between observed and calculated transition frequencies of Xe–H_2O computed in this work (TW) and the ones reported in ref. 37 (WY). Observed transitions were taken from ref. 38. Units of cm^{-1}

Level	J'–J''	Expt	TW	WY	Diff. (%) TW	Diff. (%) WY
$\Sigma(0_{00})^e$	1-0	0.1365	0.1348	0.1339	1.3	1.9
	2-1	0.2729	0.2695	0.2677	1.2	1.9
	3-2	0.4093	0.4042	0.4015	1.2	1.9
	4-3	0.5456	0.5388	0.5352	1.2	1.9
$\Sigma(1_{01})^e$	1-0	0.1338	0.1320	0.1314	1.3	1.8
	2-1	0.2676	0.2640	0.2627	1.3	1.8
	3-2	0.4013	0.3959	0.3940	1.3	1.8
	4-3	0.5351	0.5278	0.5253	1.4	1.8

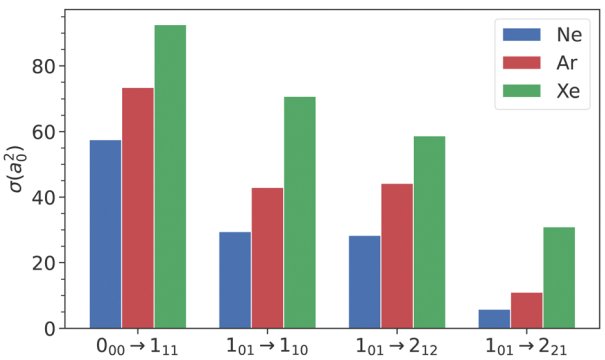

Fig. 3 Theoretical integral cross sections (ICS) for the three systems and the four transitions studied. Blue bars represent the ICS for the Ne + H_2O collision, red bars for Ar + H_2O and green bars the Xe + H_2O ones.

a given value of j, the three cases $k_a = j$, $k_a = k_c$, and $k_c = j$ correspond respectively to a rotation around the a, b, and c axes. The motion around the c axis refers to a rotation in the molecular plane while the b axis is the C_2 symmetry axis, and the a axis is perpendicular to b and c axis and parallel to the H–H axis. The $0_{00} \rightarrow 1_{11}$ transition is the only one among those measured experimentally for which the water molecule rotates around its C_2 symmetry axis in both its initial and final states but with $\Delta j = 1$. In the $1_{01} \rightarrow 2_{12}$ case the water molecule rotates in its molecular plane in both its initial and final states again with $\Delta j = 1$. Conversely, the water molecule rotation axis is not conserved during the collision for both the $1_{01} \rightarrow 1_{10}$ and $1_{01} \rightarrow 2_{21}$ transitions. The rotation initially occurs in the molecular plane around the c axis while in the final state it takes place outside of this plane around the a axis. Furthermore, the former is elastic in j while the latter is inelastic with $\Delta j = 1$.

We represent in Fig. 3 the state-selected integral cross sections (ICS) calculated for the four rotational excitation transitions studied in the present work and at the experimental collision energies. This figure gives two valuable informations. First, if we compare the ICS of the *ortho* transitions we see that they decrease monotonically when the energy of the final state increases for the three systems as expected. Conversely, the rotational excitation cross section from the fundamental to the lowest excited *para* level is seen to be larger than its *ortho* counterpart. This is rather counter intuitive as the *para* transition is inelastic in j ($\Delta j = j' - j = 1$) while the *ortho* one is elastic ($\Delta j = 0$). Furthermore, the difference of energy between the 0_{00} and 1_{11} *para* states is larger than the one between the 1_{01} and 1_{10} *ortho* states. The physical picture of this result given by the discussion of Chapman *et al.*[7] is quite appealing. As a matter of fact, the *para* transition preserves the water axis of rotation (C_2 axis) while the *ortho* transition does not, therefore suggesting that transitions which preserve the water axis of rotation are favored at this collision energy. This 'propensity rule' also explains why the $1_{01} \rightarrow 2_{12}$ cross sections are greater than those of the $1_{01} \rightarrow 2_{21}$ transition. Furthermore these two transitions which are inelastic in j give cross sections which are lower than those associated with the $1_{01} \rightarrow 1_{10}$ transition which is elastic in j.

We also clearly see, in Fig. 3, that the cross sections increase monotonically when moving from Ne to Ar and from Ar to Xe. In the Ne–Ar–Xe series, the mass, the size, and the polarizability of the atom increase. The dominant long-range electronic interactions between the Rg and H_2O are the dipole–induced dipole and the dispersion, both dependent on the Rg polarizability. The short-range repulsive interaction potential is dependent on the size of the Rg atom. As a consequence, both the potential well depth and the equilibrium bond length increase as shown by Table 5. To elucidate the trend observed in the cross sections, a classical interpretation of the phenomena is explored. It is anticipated that a deeper potential well, a more attractive long-range potential and a short-range repulsive wall located at larger inter-monomer distance are all expected to increase the maximal impact parameter, and then the cross

Table 5 Parameters of the PES for the Rg–H_2O systems and collision energies. Distances are reported in Å and energies in cm^{-1}

Rg	D_e	R_e	E_c	Ratio E_c/D_e
Ne	65.3	3.20	364	5.6
Ar	139.4	3.67	390	2.8
Xe	195.4	4.02	351	1.8

section. However the collision energies are quite larger than the depth of the potential wells (see Table 5) which is expected to reduce the effect of the attractive part of the potentials. The effect of the repulsive short-range potential is expected to play a role only for small values of the impact parameter and then to yield a small contribution to the cross section. The mass is also expected to play a role in the increase of the cross section, as shown by the classical dynamics equation

$$L_{max} = \mu v b_{max}, \quad (9)$$

where $L_{max} = J_{max} - j_{max}$ is the maximal orbital angular momentum, μ the reduced mass, v the collision relative speed and b_{max} the maximal impact parameter. In order to determine which of μ or b_{max} has the dominant effect on the cross section, we have performed a few more computations of the ICS with the following procedure. From the J_{max} values observed in the converged calculation of the ICS for the Ne + H_2O collision (see Table 1), and taking into account that j_{max} = 9 in all the calculations, we have obtained the values of b_{max} with eqn (9) and then used these latter values to calculate the values of L_{max} for the two other collisional systems Ar + H_2O and Xe + H_2O. This procedure has been applied to the ICS of the four inelastic transitions studied in the work, and the latter values of L_{max} have been used to recompute the ICS. In Table 6, we compare the values of the ICS reported in Fig. 3 and those obtained after the procedure described just above. We can see that the ICS calculated by both methods are almost equal, which shows that even with the same value of b_{max} for the three collisional systems, the cross section is still increasing in the the Ne–Ar–Xe series. This suggest that the increase of the cross section is not driven by an increase of b_{max}, but rather by the increase of the reduced mass.

The classical interpretation of the results can yield further valuable insights. Indeed, by examining the values of the total angular momentum which provide the maximum contribution to the ICS we can extract the impact parameter for which the contribution to the ICS is maximal. Those values of J associated with the transitions ($0_{00} \rightarrow 1_{11}$,$1_{01} \rightarrow 1_{10}$,$1_{01} \rightarrow 2_{12}$,$1_{01} \rightarrow 2_{21}$) correspond respectively to (33,32,33,20) in the case of Ne, (47,72,49,31) for Ar, and (67,88,70,48) for Xe. By applying the classical formula eqn (9), the b values leading to the maximum contribution to the ICS are estimated to be (1.7,1.6,1.7,0.8) Å for Ne–H_2O, (2.2,3.7,2.4,1.3) Å for Ar–H_2O, and (3.2,4.4,3.4,2.1) Å for Xe–H_2O. This suggest that at the kinetical energy of interest, for almost all the transition studied, the repulsive part of the PES contribute most to the ICS. For the transition $1_{01} \rightarrow 1_{10}$ in Ar–H_2O and Xe–H_2O, even when the b values that give the maximum contribution to the ICSs correspond to the region of the potential well, a secondary maximum structure of the ICS as a function of the J was found for smaller values of J, for which the b values also correspond to the repulsive part of the PESs, reflecting the prominent role of the short range interactions in the dynamic of the systems at the energies of interest.

Table 6 Comparison of ICS calculated by two different methods (see text). The maximum number used to calculate σ_2 is also included in the table. The number shown in parenthesis are power of ten

Rg	Transition	σ_1	σ_2	J_{max} for σ_2	Rel. error
Ar	$0_{00} \rightarrow 1_{11}$	73.6	73.6	107	1.4(−5)
	$1_{01} \rightarrow 2_{12}$	43.0	43.0	126	4.1(−5)
	$1_{01} \rightarrow 1_{10}$	44.2	44.2	97	1.3(−5)
	$1_{01} \rightarrow 2_{21}$	11.0	11.0	67	1.9(−5)
Xe	$0_{00} \rightarrow 1_{11}$	92.6	92.6	114	8.3(−5)
	$1_{01} \rightarrow 2_{12}$	70.7	70.7	135	1.4(−4)
	$1_{01} \rightarrow 1_{10}$	58.7	58.7	103	2.7(−5)
	$1_{01} \rightarrow 2_{21}$	30.9	30.7	71	8.6(−3)

New theoretical ICSs calculations, performed for the same collision energies but for transitions from the fundamental *para* (0_{00}) and *ortho* (1_{01}) levels of H_2O to some selected final states, not studied experimentally, are presented in Fig. 4. The final states were chosen to compare the three principal alignment cases discussed by Chapman *et al.*[7] In their work, the authors observed strong alignment effects of the products when studying the excitation of H_2O by collision with Ar at a collision energy of 480 cm^{-1}. For Both of the two *ortho*/*para* spin symmetries, they noticed that, for a given final j value, the largest ICSs are obtained for the $\Delta j = \Delta k_a$ or $\Delta j = \Delta k_c$ transitions while those associated with $\Delta k_a = \Delta k_c$ give significantly smaller ICSs. As can be seen in Fig. 4, the transitions calculated for these three different systems follow the same propensity rules as the $\Delta k_a = \Delta k_c$ ICS are seen to be one order of magnitude smaller than those of the two other cases. It can therefore be conclude that the propensity rule discussed by Chapman *et al.*[7] for the excitation of H_2O by Ar is also valid for other H_2O + Rg systems.

3.4 Differential cross sections

In the present work, we report rotationally resolved state-to-state differential cross sections of H_2O colliding with rare gas atoms in the centre-of-mass frame which have been acquired for the first time. A series of background-subtracted raw velocity mapped H_2O^+ images measured for the H_2O + Ne, H_2O + Ar, H_2O + Xe systems at the respective collision energy of 364, 390 and 351 cm^{-1} is presented in Fig. 5, along with the corresponding Newton diagrams. With respect to the relevant velocity vectors indicated by the red dashed lines in the diagrams, the directions of the scattered products can be described as forward, sideway and backward scattering in the center-of-mass frame. In these false-color images, it is apparent that the intensity is higher in the forward and sideway scattering direction in most cases. Meanwhile all the images clearly display asymmetric angular distributions with respective to their relative velocity axes, shown as the red dashed arrows superimposed on the raw images in the figure, due to the measurement of laboratory product density instead of flux. Using the IMSIM[19]

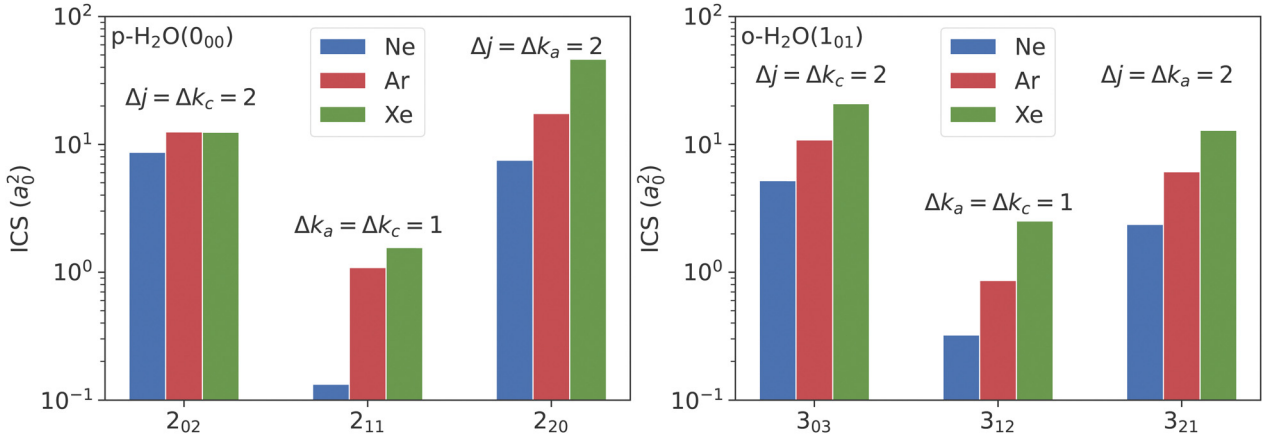

Fig. 4 Theoretical integral cross sections (ICS) for the excitation of the fundamental *para* level (left plot) and *ortho* level of H_2O by collision with rare gases. Blue bars represent the ICS for the Ne + H_2O collision, red bars for Ar + H_2O and green bars the Xe + H_2O ones. The selected final states correspond to three different alignment cases: $\Delta j = \Delta k_a$ (rotation along the *a* molecular axis), $\Delta k_a = \Delta k_c$ (Rotation along the *b* molecular axis) and $\Delta j = \Delta k_c$ (Rotation along the *c* molecular axis).

simulation program, "apparatus function" was first simulated with the input of an assumed isotropic DCS together with all the experimental parameters, such as geometry and spatial conditions of incident molecular beams and laser beam, temporal and velocity distribution of molecular beams and so on. Then the state-to-state differential cross sections were obtained using the experimental angular distributions of the background-subtracted raw images divided by the corresponding apparatus function and finally normalized for comparison with calculations.

Theoretically, the DCSs were calculated for the collisions of H_2O with Ne, Ar and Xe for the transitions that were experimentally measured. The collision energies were respectively 364 cm^{-1}, 390 cm^{-1}, and 351 cm^{-1}. Given the numerous oscillations inherent to the theoretical DCS, we also computed convoluted DCS with experimental angular spread. We use a Gaussian function

$$f(x) = \frac{1}{\sigma\sqrt{2\pi}} \exp\left[-\frac{1}{2}\left(\frac{x}{\sigma}\right)^2\right]$$

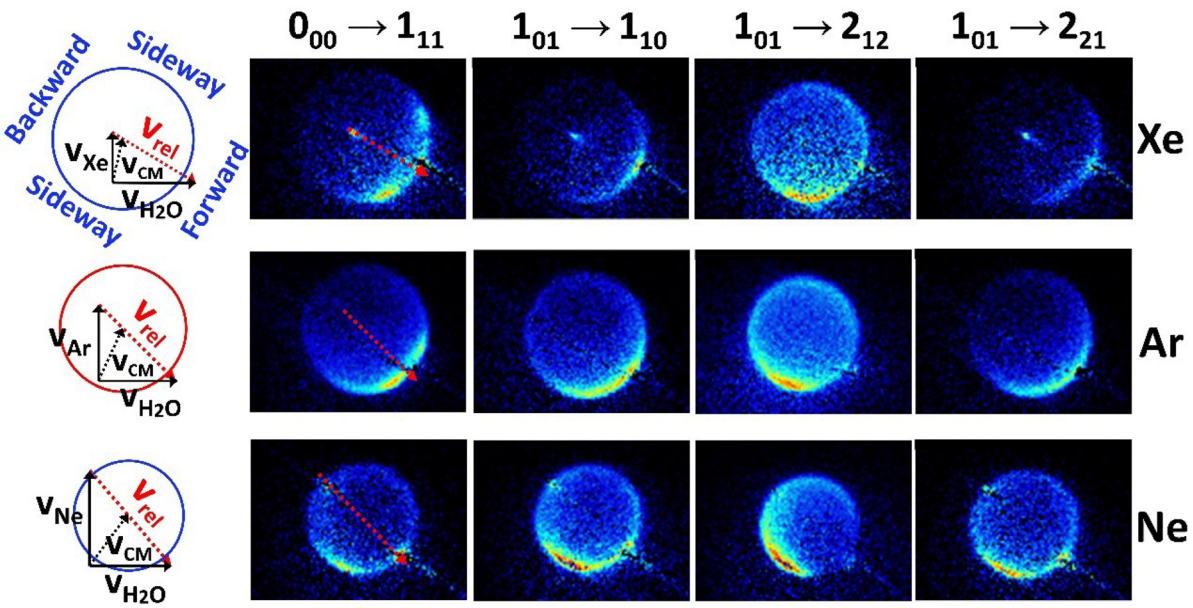

Fig. 5 Background subtracted images of inelastically scattered H_2O in the indicated rotational transitions for collisions of H_2O with Xe (top row), Ar (middle row) and Ne (bottom row). The corresponding Newton diagrams for the three colliding systems are shown on the left side of this figure. v_{H_2O} represents the velocity of H_2O in the primary molecular beam (black arrow in horizontal direction); v_{Xe}, v_{Ar} and v_{Ne} represents the velocity of the Xenon, Argon and Neon in the secondary beam (black arrow in vertical direction), respectively. The black dashed arrows indicate the center of mass velocity v_{CM} and the red dashed arrows indicate the relative velocity v_{rel} for three colliding systems. Same red dashed arrows are superimposed on the corresponding H_2O images for better visualization. The blue circles indicate the size (not scaled exactly) of the Newton sphere for inelastic scattering and the directions described as forward, sideway and backward scattering in the center-of-mass frame (0°, 90°, and 180° in the DCS plotted in the Figure).

to model the spread, being x the deflection angle, with standard deviation $\sigma = 15^\circ$ for $\theta \leq 10^\circ$ and $\sigma = 5^\circ$ for the rest of the angular interval. In order to allow comparing the experimental and theoretical values of the DCS on the same figure, we equate them at $\theta = 100^\circ$. This angle was selected based on the observation that the theoretical DCS exhibits a reduced number of oscillations around this angle when compared to the DCS at smaller angles.

For the collision with Ne three of the four transitions DCS presented in Fig. 6 are predicted, by the theoretical calculation, to be strongly forward, while the $1_{01} \rightarrow 2_{21}$ transition is the only one with an important backward contribution. At small deflection angles, the agreement between theory and experiment is not good, due most probably to the subtraction procedure of the background signal from the unscattered beam. For the rest of the angular interval, the agreement becomes quite satisfactory. The theoretical calculations are in excellent agreement with the experimental observations of the monotonic increase of the $1_{01} \rightarrow 2_{21}$ DCS above 20°.

The DCSs for the collision with Ar are presented in Fig. 7. The general agreement between theory and experiment is also good for this system. The theoretical results reproduce the main shapes observed in the experiments, with the $1_{01} \rightarrow 1_{10}$ being almost perfectly described, even better if we compare the convoluted cross sections. Again, appreciable discrepancies between theory and experiment are for the same reasons observed only for small deflection angles, with the exception of the $1_{01} \rightarrow 2_{21}$ transition, for which the theoretical backscattering is overestimated for angles larger than 120°. This constitutes one of two noteworthy distinctions in behaviour between the Ne + H_2O and Ar + H_2O DCS. The first one is the bump around 35° which can be observed in the Ar + H_2O DCS and is correctly predicted by the calculations, while the second is the decrease of the backscattering in the Ar + H_2O DCS for the larger angles, which is not reproduced by the calculations.

In order to further analyse this difference between these two systems, we report in Fig. 9 the contributions to the DCS associated with all the possible initial (m) and final (m') values of the SF z-axis projection of the water angular momentum (see eqn (7)). As can be seen in this figure, the main contribution to backward scattering is for both systems due to the $m = 1 \rightarrow m' = 1$ component for this transition. In other words, the largest backward contribution to the DCS is due to collisions conserving the water SF j_z quantum number. This also means that $m_l' = 0$ (see eqn (8)) and that the SF z-axis is along the final intermolecular axis which is also the final relative velocity vector and the final body-fixed z-axis. In other words, the SF z-axis which is defined by the direction of the initial incoming relative velocity is in coincidence with the final body-fixed z-axis and is conserved during the collision. This suggest that the angular potential expansion coefficients $v_{l,m=0}(R)$ (Fig. 8) are giving the largest contributions to this particular state to state DCS in the backward angular range. We can conclude that the $v_{l,m=0}(R)$ components of the potential leading to backward scattering for the $1_{01} \rightarrow 2_{21}$ transition in the Ar + H_2O collision are probably not accurate enough.

The theoretical and experimental results for Xe, presented in Fig. 10, demonstrate excellent qualitative and quantitative alignment. The three peaks observed observed in the $1_{01} \rightarrow 1_{10}$ DCS experiment are qualitatively reproduced by the theoretical calculations. A minor discrepancy is observed between the theoretical and experimental third peaks, with the former being

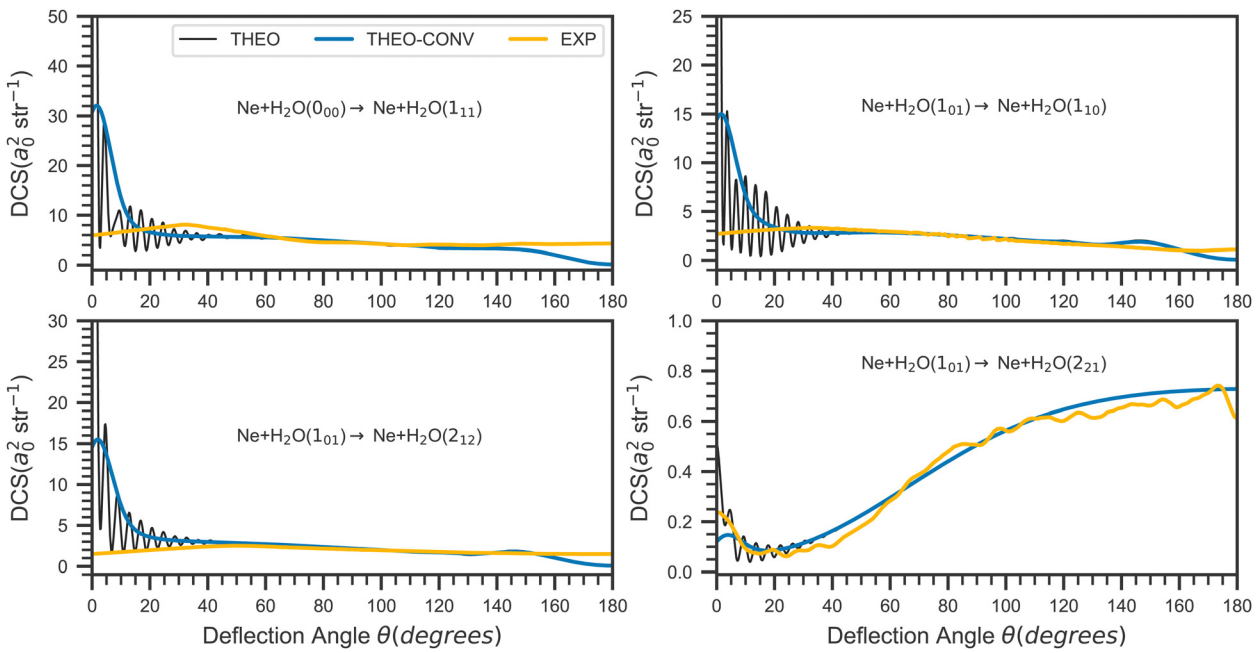

Fig. 6 State-to-state differential cross sections (DCS) for four different rotational transitions of the water molecule induced by the collision with the Ne atom. The $0_{00} \rightarrow 1_{11}$, $1_{01} \rightarrow 1_{10}$, $1_{01} \rightarrow 2_{12}$, and $1_{01} \rightarrow 2_{21}$ transitions are presented in top-left, top-right, bottom-left, and bottom-right panels respectively. Black lines correspond to the theoretical results, yellow lines to the experimental results, and blue lines are the convoluted theoretical results using a Gaussian function.

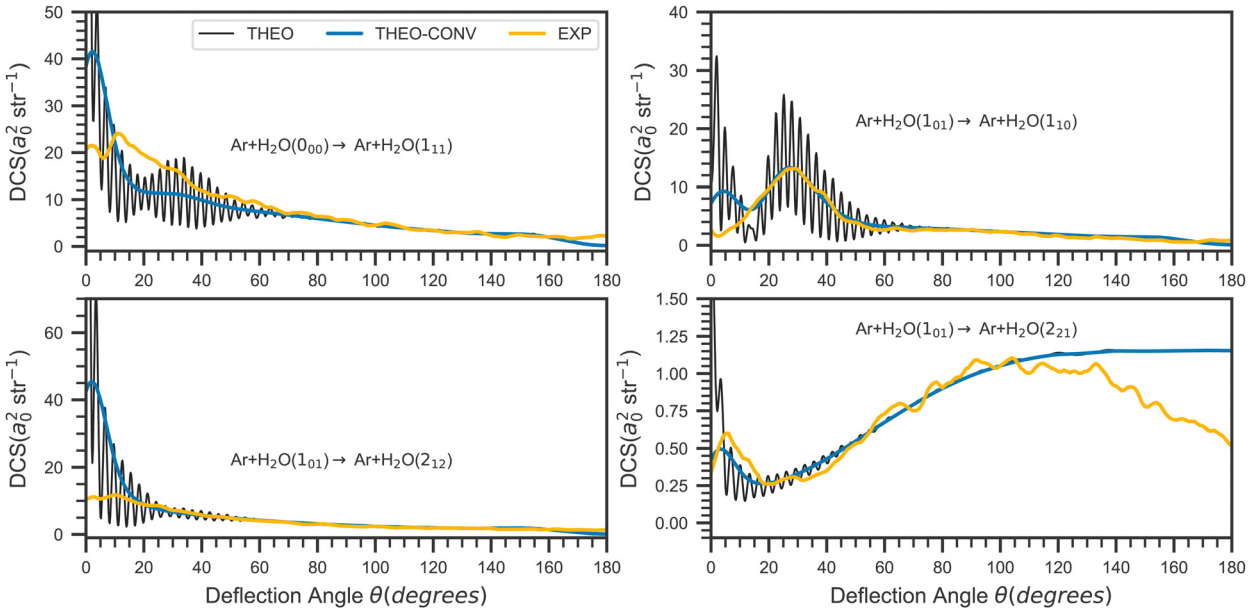

Fig. 7 Same as Fig. 6 but for the H_2O + Ar collision.

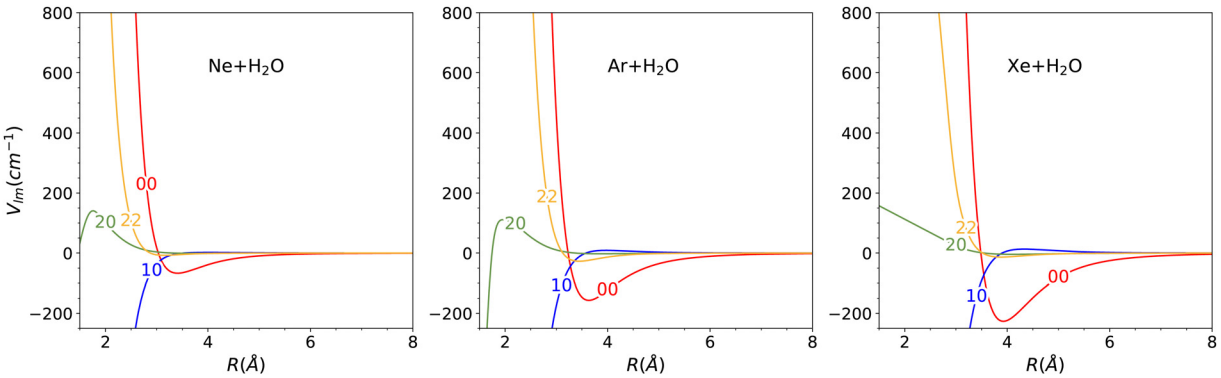

Fig. 8 Partial wave expansion coefficients of the PES ($v_{l,m}$) as a function of R for Ne + H_2O (left panel), Ar + H_2O (middle panel) and Xe + H_2O (right panel). The partial wave numbers are indicated in each curve, and only the four first partial waves are presented.

shifted to the right. The number of oscillations of the DCS is the highest observed among the three systems. The increase in the number of oscillations is associated with the increase of the system's reduced mass, which requires higher values of J for the DCS to converge. Furthermore, the collision energies are quite larger than the dissociation energies, thus reducing contributions of the potential well region to the dynamics. It is rather the short range region of the PES that is in control of the dynamics at these energies.

All the calculated DCSs reported in this work show fast oscillations for small angles of diffusion. We can interpret these oscillations with a simple picture. The hard sphere model predicts narrow Fraunhofer forward diffraction peaks of the DCS resulting from interference between the incident wave and the outgoing scattered wave. An equivalent quantum interpretation of these rapid oscillations suggests that they are the result of interference between the numerous partial waves that contribute to the inelastic DCSs. The calculated $\Delta\theta$ spacing between the diffraction oscillations is roughly estimated to be 4.2°, 2.8° and 2.4° respectively for the collisions of H_2O with Ne, Ar and Xe. Using the hard sphere scattering formula $\Delta\theta = \frac{\pi}{kR_0}$ where $k = \sqrt{2\mu E_C}/\hbar$, and R_0 is the size of the collision complex at closest approach, we obtain for these three systems respectively R_0 = 2.98, 3.79 and 4.13 Å which is in qualitative agreement with the equilibrium separations of H_2O and the rare gas.

Super imposed on this fast oscillations the DCSs exhibit broad rotational rainbow maximum which are most visible in the $1_{01} \rightarrow 1_{10}$ DCS for Ar + H_2O in Fig. 7 and Xe + H_2O in Fig. 10. The semi-classical picture of rainbow scattering is that they stem from interferences of trajectories with different impact parameters leading to the same deflection angle and rotational angular momentum transfer $\Delta j = j' - j$.

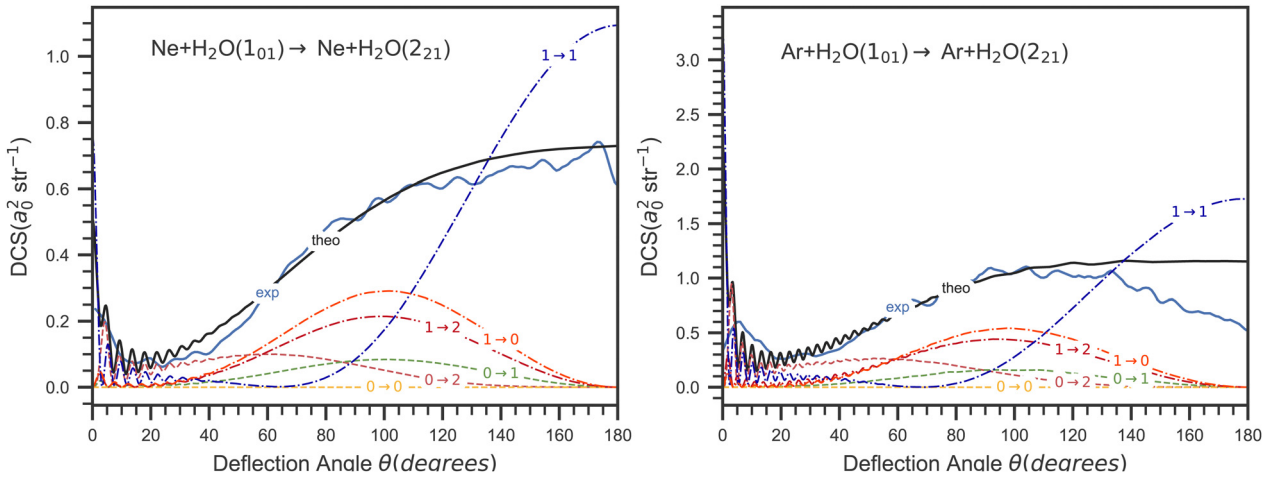

Fig. 9 Comparison of the $m_i \rightarrow m_f$ state selected contributions to the $1_{01} \rightarrow 2_{21}$ DCS transition of water by collision with Ne (left panel) and Ar (right panel). The initial m_i and final m_f values of the z SF projection of the water rotational angular momentum are reported on each curve (Dashed lines) associated with a partial $m_i \rightarrow m_f$ contribution. The experimental and summed theoretical DCS are also represented using solid black and red lines, respectively.

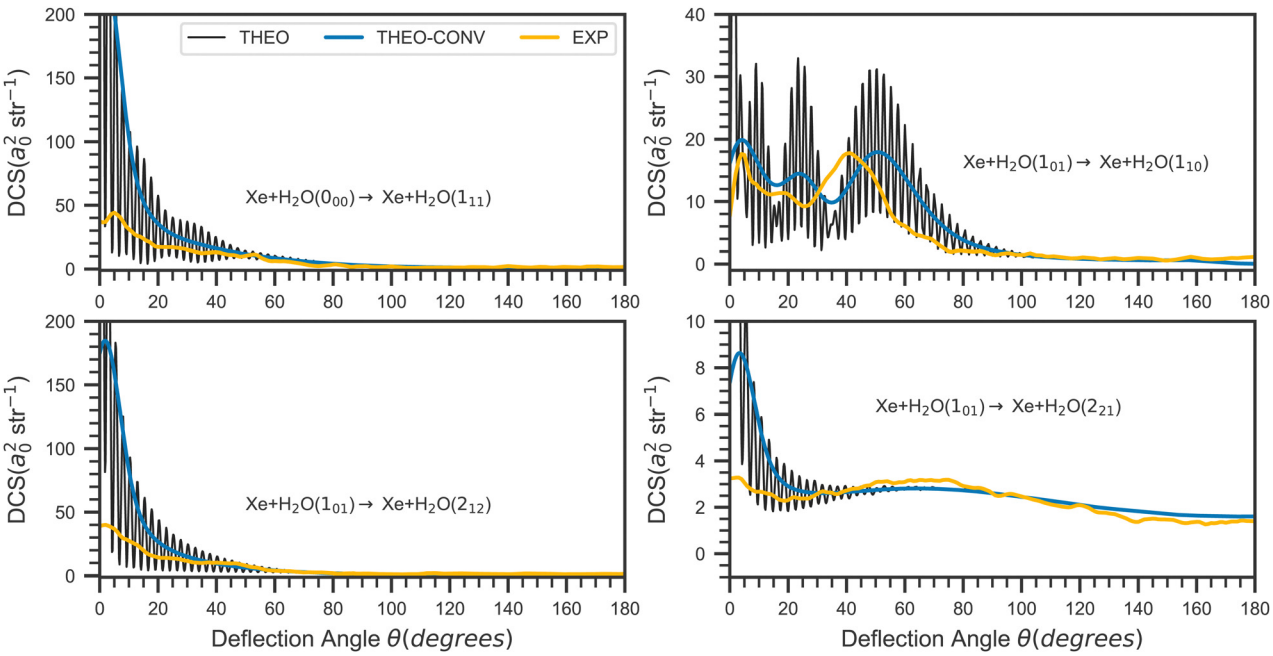

Fig. 10 Same as Fig. 6 but for the H_2O + Xe collision.

Conclusions

We presented a combined experimental and theoretical study of the DCSs for the inelastic collisions of water with three rare gases atoms: Ne, Ar and Xe. The experimental study was carried out in a crossed molecular beam and VMI setup with state-selective laser ionization detection. Water molecules are cooled by adiabatic expansion before collision, and each of the two species, *ortho* and *para*-H_2O, are mostly in their respective ground states, namely 0_{00} and 1_{01}. VMI detection of the water molecules by means of (2 + 1) REMPI allowed to measure the rotationally excited states of H_2O products as a function of the scattering angle, resulting in the state-to-state DCS measured experimentally.

On the theoretical side, a new PES was built for the Xe + H_2O system and the bound states of this system calculated. The calculated transition frequencies of the Xe + H_2O complex using this PES are in excellent agreement with experimental data and show slight improvement over previous calculations. We use for the two remaining systems (Ne + H_2O and Ar + H_2O) two PESs that we recently developed and tested.

The calculated ICS increases with the mass of the rare gas atom. This is due to the increase of the rare gas polarizability

along with the increase of both the dissociation energy and the reduced mass of the Rg + H_2O complex. A strong alignment effect is observed for the ICS. The results for the three Rg cases are consistent with the propensity rule observed by Chapman-1999[7] for H_2O + Ar collisions at 480 cm^{-1}. This finding indicates that this propensity rule may be a general principle that governs the rotational excitation of H_2O by collisions with rare gases at relatively high collision energies.

The calculated and measured DCSs for the three systems are in good agreement, except for small deflection angles of most DCSs and for the backward scattering in the transition $1_{01} \rightarrow 2_{21}$ of the collision with Ar. The former is likely attributable to the subtraction procedure of the background signal from the unscattered beam while the latter might be due to inaccuracies in the repulsive part of the PES.

The narrow Fraunhofer forward diffraction peaks of the DCS are observed theoretically for the three systems. Furthermore, the sizes of the collision complexes at closest approach predicted by the hard sphere model are in qualitative agreement with the equilibrium separation between H_2O and the rare gas as given by the PESs. Super imposed on this fast oscillations the DCSs exhibit broad rotational rainbow maxima which are most visible in the $1_{01} \rightarrow 1_{10}$ DCS for Ar + H_2O and Xe + H_2O.

In the case of the Ar + H_2O collisions, the theoretical $1_{01} \rightarrow 2_{21}$ DCS backscattering is overestimated for angles larger than 120°. This may be due to inaccuracies of either the experimental measurement in this angular region or in the repulsive part of the PES developed for this system. In order to answer this question and to test other collision energy ranges, new measurements and calculations are required. This will enable the testing of other regions of the PESs.

Data availability

Data for this article, including data files and jupyter notebooks used to generate the plots are available at the **https://figshare.com/** repository at **https://doi.org/10.6084/m9.figshare.28078265**.

Conflicts of interest

There are no conflicts to declare.

Acknowledgements

This work was supported by the French Agence Nationale de la Recherche (ANR-Waterstars), Contract No. ANR-20-CE31-0011, the National Natural Science Foundation of China (Grant No. 22103003) and the Anhui Provincial Natural Science Foundation (Grant No. 2208085Y02). We acknowledge the support from the ECOS-SUD-ANID project number C22E02 (Programa de Cooperación Científica ECOS-ANID ECOS220023). Computer time for this study was provided by the Mésocentre de Calcul Intensif Aquitaine, which is the computing facility of Université de Bordeaux et Université de Pau et des Pays de l'Adour.

References

1 C. Xiahou, J. N. L. Connor, D. De Fazio and D. Sokolovski, *Phys. Chem. Chem. Phys.*, 2024, **26**, 3647–3666.
2 O. Tkáč, A. K. Saha, J. Loreau, D. H. Parker, A. van der Avoird and A. J. Orr-Ewing, *J. Phys. Chem. A*, 2015, **119**, 5979–5987.
3 G. Sarma, A. K. Saha, C. K. Bishwakarma, R. Scheidsbach, C.-H. Yang, D. Parker, L. Wiesenfeld, U. Buck, L. Mavridis and S. Marinakis, *Phys. Chem. Chem. Phys.*, 2017, **19**, 4678–4687.
4 R. W. Bickes, G. Duquette, C. J. V. D. Meijdenberg, A. M. Rulis, G. Scoles and K. M. Smith, *J. Phys. B: At., Mol. Opt. Phys.*, 1975, **8**, 3034–3043.
5 J. T. Slankas, M. Keil and A. Kuppermann, *J. Chem. Phys.*, 1979, **70**, 1482–1491.
6 J. Brudermann, C. Steinbach, U. Buck, K. Patkowski and R. Moszynski, *J. Chem. Phys.*, 2002, **117**, 11166–11174.
7 W. B. Chapman, A. Kulcke, B. W. Blackmon and D. J. Nesbitt, *J. Chem. Phys.*, 1999, **110**, 8543–8554.
8 V. Aquilanti, E. Cornicchi, M. Moix Teixidor, N. Saendig, F. Pirani and D. Cappelletti, *Angew. Chem., Int. Ed.*, 2005, **44**, 2356–2360.
9 F. Pirani, L. F. Roncaratti, L. Belpassi, F. Tarantelli and D. Cappelletti, *J. Chem. Phys.*, 2011, **135**, 194301.
10 C.-H. Yang, G. Sarma, J. J. ter Meulen, D. H. Parker, U. Buck and L. Wiesenfeld, *J. Phys. Chem. A*, 2010, **114**, 9886–9892.
11 C.-H. Yang, J. J. ter Meulen, D. H. Parker and C. M. Western, *Phys. Chem. Chem. Phys.*, 2010, **12**, 13983–13991.
12 G. Sarma, A. K. Saha, C. K. Bishwakarma, R. Scheidsbach, C.-H. Yang, D. H. Parker, L. Wiesenfeld, U. Buck, L. Mavridis and S. Marinakis, *Phys. Chem. Chem. Phys.*, 2017, **19**, 4678.
13 C.-H. Yang, G. Sarma, D. H. Parker, J. J. ter Meulen and L. Wiesenfeld, *J. Chem. Phys.*, 2011, **134**, 204308.
14 R. M. García-Vázquez, O. Denis-Alpizar and T. Stoecklin, *J. Phys. Chem. A*, 2023, **127**, 4838–4847.
15 R. M. García-Vázquez, L. D. Cabrera-González, O. Denis-Alpizar and T. Stoecklin, *ChemPhysChem*, 2024, **25**, e202300752.
16 C.-H. Yang, G. Sarma, J. J. ter Meulen, D. H. Parker, G. C. McBane, L. Wiesenfeld, A. Faure, Y. Scribano and N. Feautrier, *J. Chem. Phys.*, 2010, **133**, 131103.
17 K. T. Lorenz, M. S. Westley and D. W. Chandler, *Phys. Chem. Chem. Phys.*, 2000, **2**, 481.
18 Z.-F. Sun, C. K. Bishwakarma, L. Song, A. van der Avoird, M. C. van Hemert, A. G. Suits, G. C. McBane and D. H. Parker, *Phys. Chem. Chem. Phys.*, 2019, **21**, 9200–9211.
19 G. C. McBane, *Imsim: A program for simulating images from crossed-beam scattering experiments with laser photoionization and 2D velocity mapping detection, version 3.0*, 2018, **https://faculty.gvsu.edu/mcbaneg/**.
20 H.-J. Werner, P. J. Knowles, G. Knizia, F. R. Manby and M. Schütz, *Wiley Interdiscip. Rev.: Comput. Mol. Sci.*, 2012, **2**, 242–253.
21 S. M. Cybulski and R. Toczyłowski, *J. Chem. Phys.*, 1999, **111**, 10520.
22 L. Wiesenfeld, Y. Scribano and A. Faure, *Phys. Chem. Chem. Phys.*, 2011, **13**, 8230–8235.
23 S. Green, *J. Chem. Phys.*, 1976, **64**, 3463–3473.

24 P. Soldán and J. M. Hutson, *J. Chem. Phys.*, 2000, **112**, 4415–4416.
25 L. D. Cabrera-González, O. Denis-Alpizar, D. Páez-Hernández and T. Stoecklin, *Mon. Not. R. Astron. Soc.*, 2022, **514**, 4426–4432.
26 T. Stoecklin, L. D. Cabrera-González, O. Denis-Alpizar and D. Páez-Hernández, *J. Chem. Phys.*, 2021, **154**, 144307.
27 D. Hou, Y.-T. Ma, X.-L. Zhang and H. Li, *J. Chem. Phys.*, 2016, **144**, 014301.
28 L. Liu, D. Yang, H. Guo and D. Xie, *J. Phys. Chem. A*, 2023, **127**, 195–202.
29 D. Hou, Y.-T. Ma, X.-L. Zhang and H. Li, *J. Mol. Spectrosc.*, 2016, **330**, 217–227.
30 T. Stoecklin, O. Denis-Alpizar, A. Clergerie, P. Halvick, A. Faure and Y. Scribano, *J. Phys. Chem. A*, 2019, **123**, 5704–5712.
31 R. M. García-Vázquez, A. Bergeat, O. Denis-Alpizar, A. Faure, T. Stoecklin and S. B. Morales, *Faraday Discuss.*, 2024, **251**, 205–224.
32 R. N. Zare, *Angular Momentum*, Wiley, New York, 1988.
33 M. W. Chase Jr., *NIST-JANAF Thermochemical Tables*, J. Phys. Chem. Ref. Data, Monograph 9, Washington, DC, 1998, 4th edn, pp. 1–1951.
34 D. E. Manolopoulos, PhD thesis, University of Cambridge, 1988.
35 D. E. Manolopoulos, *J. Chem. Phys.*, 1986, **85**, 6425–6429.
36 R. M. García-Vázquez, L. D. Cabrera-González, O. D. Alpizar and T. Stoecklin, *ChemPhysChem*, 2024, **25**, e202400353.
37 L. Wang and M. Yang, *J. Chem. Phys.*, 2008, **129**, 174305.
38 Q. Wen and W. Jäger, *J. Phys. Chem. A*, 2006, **110**, 7560–7567.